TU Delft

Delft University of Technology

Document Version
Final published version

Licence
CC BY-NC-ND

Citation (APA)
Ungerer, J. H., Pally, A., Bosco, S., Kononov, A., Sarmah, D., Lehmann, S., Thelander, C., Maisi, V. F., Scarlino, P., & More Authors (2025). A dephasing sweet spot with enhanced dipolar coupling. *Communications Physics*, *8*(1), Article 306. https://doi.org/10.1038/s42005-025-02216-9

Important note
To cite this publication, please use the final published version (if applicable).
Please check the document version above.

Copyright
In case the licence states “Dutch Copyright Act (Article 25fa)”, this publication was made available Green Open Access via the TU Delft Institutional Repository pursuant to Dutch Copyright Act (Article 25fa, the Taverne amendment). This provision does not affect copyright ownership.
Unless copyright is transferred by contract or statute, it remains with the copyright holder.

Sharing and reuse
Other than for strictly personal use, it is not permitted to download, forward or distribute the text or part of it, without the consent of the author(s) and/or copyright holder(s), unless the work is under an open content license such as Creative Commons.

Takedown policy
Please contact us and provide details if you believe this document breaches copyrights.
We will remove access to the work immediately and investigate your claim.

This work is downloaded from Delft University of Technology.

communications physics

A Nature Portfolio journal

Article

https://doi.org/10.1038/s42005-025-02216-9

A dephasing sweet spot with enhanced dipolar coupling

Check for updates

Jann H. Ungerer[1,2,3,8] ✉, Alessia Pally[2,8], Stefano Bosco[4], Artem Kononov[2], Deepankar Sarmah[2], Sebastian Lehmann[5], Claes Thelander[5], Ville F. Maisi[5], Pasquale Scarlino[6], Daniel Loss[2], Andreas Baumgartner[1,2] & Christian Schönenberger[1,2,7]

Two-level systems (TLSs) are the basic units of quantum computers but face a trade-off between operation speed and coherence due to shared coupling paths. Here, we investigate a TLS given by a singlet-triplet (ST+) transition. We identify a magnetic-field configuration that maximizes dipole coupling while minimizing total dephasing, forming a compromise-free sweet spot that mitigates this fundamental trade-off. The TLS is implemented in a crystal-phase-defined double-quantum dot in an InAs nanowire. Using a superconducting resonator, we measure the spin-orbit interaction (SOI) gap, the spin-photon coupling strength, and the total TLS dephasing rate as a function of the in-plane magnetic-field orientation. Our theoretical description postulates phonons as the dominant noise source. The compromise-free sweet spot originates from the SOI, suggesting that it is not restricted to this material platform but might find applications in any material with SOI. These findings pave the way for enhanced nanomaterial engineering for next-generation qubit technologies.

Qubits based on single localized spins in semiconductor nanostructures represent cutting-edge platforms for quantum information processing, boasting extended coherence times and benefiting from established industrial fabrication techniques[1]. Scaling-up spin qubits is challenging because of limitations in all-electrical control and their small electric and magnetic dipole moments. Complex structures such as microstrips or micromagnets are required to facilitate qubit manipulation[2,3]. However, the inherent spin-orbit interaction (SOI) in confined semiconductor hole systems[4–8] and in electrons in nanowires (NWs)[9–13] offers an alternative coupling mechanism: SOI couples spin and charge degrees of freedom, enabling electric-dipole spin resonance[14–17] and spin-cavity coupling[9,11,13,18–23].

SOI is particularly relevant in singlet-triplet qubits, where it introduces a hybridization gap, for example, between singlet $|S\rangle$ and spin-polarized triplet $|T^+\rangle$ states[24–26]. Recent experiments have demonstrated gigahertz-scale gaps, allowing for reaching the strong coupling limit between these two-level systems and microwave resonators[22]. These experiments extended the list of systems with strong spin-photon coupling[21,27–29] to even charge-parity states.

Despite several reports of SOI-induced material characteristics as a function of the magnetic field orientation[13,21,30–32], typically, sweet spots optimize coherence and manipulation speed as a function of gate voltages in charge qubits around zero detuning[33,34], which was recently extended to single-spin spin qubit[35]. Here, we demonstrate that, while remaining at the gate-voltage sweet spot, an additional sweet spot for the total dephasing rate and dipole strength can be found, namely as a function of the orientation of a homogeneous in-plane magnetic field. As the fundamental origin of this additional sweet spot, we identify the inherently strong spin-orbit interaction (SOI) in the host material.

We do so by employing a two-spin singlet-triplet (S-T^+) TLS in a crystal-phase-defined InAs NW[22,36,37] coupled to a NbTiN resonator[38,39] that is resilient to in-plane magnetic fields. Due to its spin nature, the TLS strongly depends on the magnetic-field orientation. We investigate the TLS properties as a function of the in-plane magnetic field in different orientations relative to the double quantum dot (DQD)[13,21,30,40] which acts like a one-dimensional, global tuning parameter. The coupling between the singlet-triplet TLS and the resonator allows to measure the TLS transition frequency, the vacuum Rabi rate, and the total TLS dephasing rate. Contrary to prevailing expectations, we identify a magnetic field orientation along the nanowire that serves as a compromise-free sweet spot, where a minimal total dephasing rate coincides with a maximal dipolar coupling. These findings are well explained by a theoretical model that suggests phonons as the dominant source of decoherence.

This non-trivial optimization of two TLS parameters with only one external parameter is inherent to systems with a strong SOI and

[1]Swiss Nanoscience Institute, University of Basel, Basel, Switzerland. [2]Department of Physics, University of Basel, Basel, Switzerland. [3]Department of Physics, Harvard University, Cambridge, MA, USA. [4]QuTech and Kavli Institute of Nanoscience, Delft University of Technology, Delft, Netherlands. [5]Solid State Physics and NanoLund, Lund University, Lund, Sweden. [6]Institute of Physics and Center for Quantum Science and Engineering, Ecole Polytechnique Fédérale de Lausanne, Lausanne, Switzerland. [7]https://www.nanoelectronics.ch. [8]These authors contributed equally: Jann H. Ungerer, Alessia Pally. ✉e-mail: jungerer@fas.harvard.edu

demonstrates the potential of such semiconductor materials. Our results pave the way for future advances in material optimization and enhanced device functionality based on a deeper understanding of the underlying physics.

Results and Discussion

Device

The device is depicted in Fig. 1. Detailed fabrication procedures are outlined in the Methods. This device comprises a superconducting half-wavelength coplanar-waveguide resonator coupled to a DQD formed by in-situ crystal-phase engineering in an InAs NW[22,36,37,41]. Figure 1a shows an optical microscopy image of the resonator, fabricated by dry-etching an approximately 10 nm thick NbTiN film, atop a SiO_2 substrate[39]. The small thickness of the superconducting NbTiN renders the resonator resilient to in-plane magnetic fields[38,39], and the narrow center conductor width, approximately 380 nm, combined with the large kinetic inductance of NbTiN, results in an impedance of 2.1 kΩ. This large impedance enhances the vacuum electric field fluctuation amplitude compared to standard 50 Ω-type resonators, thereby increasing the dipolar coupling to the TLS[42].

The TLS is formed by electronic states in a DQD, with tunnel barriers grown deterministically by controlling the InAs crystal phase during the vertical growth process of the NW[36,37]. The barriers are highlighted in the colored SEM image of Fig. 1b in red. The DQD forms within the zincblende segments of the NW, separated by wurtzite tunnel barriers. At finite magnetic fields and in an even electron configuration, the DQD states are singlet and triplet states, as depicted in the energy level diagram in Fig. 1c. The ground state and first excited state comprise a superposition of the spin-polarized triplet $|T^+\rangle$, with an electron on each dot and the low-energy singlet state $|S_{2,0}\rangle$, with two excess electrons on one dot and none on the other. As depicted in Fig. 1c, without spin-flip tunneling, the energy levels would cross at a detuning ε_0 at which the Zeeman energy E_z equals the exchange energy $\hbar J$,

$$E_z = \hbar J \approx \frac{\hbar}{2}\left(\varepsilon_0 + \sqrt{\varepsilon_0^2 + 4t_c^2}\right), \tag{1}$$

where t_c is the inter-dot tunnel rate and $\hbar$ denotes the reduced Planck constant. But the finite inter-dot tunnel coupling and a substantial Rashba-type SOI in the zincblende segments[41] result in a spin rotation and in the hybridization of the original eigenstates, with an energy gap $\hbar\Delta_{so}$[24]. The two hybridized spin levels are split by a spin-orbit gap and constitute a spin-orbit-mediated electric dipole moment that couples to the electric field fluctuations of the resonator. This renders the resonator an effective probe for quantitative measurements of the TLS parameters.

Hybrid system at large magnetic fields

In our experiments, we measure the amplitude A and phase φ of a microwave probe tone transmitted through the resonator, capacitively coupled to the DQD. All measurements are performed at the mixing chamber plate of a dilution refrigerator with a base temperature of 70 mK. In Fig. 2a, the squared normalized transmission amplitude $(A/A_0)^2$ through the resonator is plotted as a function of the probe frequency ω_p with the DQD tuned into Coulomb blockade, rendering it irrelevant for the measurement. This figure displays probe frequency scans at magnetic-field amplitudes $|\mathbf{B}| = 0$ mT and $|\mathbf{B}| = 100$ mT, where the field is applied in-plane. As visible in Fig. 2(a), the transmission through the resonator recorded for $|\mathbf{B}| = 0$ mT and $|\mathbf{B}| = 100$ mT does not show any variation, demonstrating that the resonator remains unaffected for the magnetic fields used in our experiments.

We now prepare the DQD in an even charge state[22,43–45] and measure the resonator transmission at a frequency close to resonance. Figure 2b–e depict the transmission amplitude and phase as functions of the gate voltages V_L and V_R for in-plane field amplitudes of $|\mathbf{B}| = 0$ and $|\mathbf{B}| = 100$ mT.

Due to the electric-dipolar coupling between the resonator and the DQD, the resonator transmission directly reveals the charge stability diagram of the DQD[46]. At the inter-dot transition (IDT), the Zeeman energy and the exchange energy are degenerate (see Eq. (1)) and the hybridized states couple to the resonator. The IDT can be easily identified, signaled by lines with positive slopes in Fig. 2e.

Both, the position of the IDT in the gate-versus-gate map and the resonator response near the IDT strongly depend on the external magnetic field strength. This susceptibility to magnetic fields arises from the spin-dependent DQD transitions. In the following, we probe the resonator response as a function of electrostatic detuning ε, which is manipulated by varying the gate voltages V_L and V_R along the line indicated in Fig. 2e.

A double sweet spot

The main result of our work is represented by the dependence of the IDT characteristics on the in-plane field orientation. For this we show in Fig. 3a the resonator transmission phase φ close to the resonance frequency, plotted as a function of the in-plane angle α between the NW axis and the magnetic field, illustrated in Fig. 1b and Fig. 3b, and versus the electrostatic DQD detuning ε as defined in Fig. 2e. Similar data for varying magnetic field strength is shown in the SM. Figure 3a reveals that the detuning ε_0, at which the IDT is observed, varies as a function of α. This angle dependence can be understood qualitatively by recognizing that the SOI introduces an anisotropic g-tensor and hence determines the Zeeman energy E_Z and, according to Eq. (1), the position of the IDT ε_0. Furthermore, the phase signal as a function of ε changes continuously from a negative shift in φ at $\alpha \approx \pi/2$ [$3\pi/2$] to a double-dip structure at $\alpha \approx \pi$ [2π], because the SOI renders the magnitude of Δ_{SO} and the dephasing rate γ angle-dependent by affecting the overlap of the spin wavefunctions[24,30,40,47]. For example, at $\alpha \approx \pi/2$, $\Delta_{so} > \omega_0$, resulting in a dispersive resonator signal. In contrast, at $\alpha \approx \pi$, $\Delta_{so} < \omega_0$ so that an (avoided) crossing between the singlet-triplet TLS and the resonator is observed as function of ε. This crossing experimentally results in a double dip structure in the $\varphi(\varepsilon)$ dependence, framing a positive shift at the center of the IDT, at $\varepsilon \approx \varepsilon_0$.

Using input-output theory[48] as described in the Methods, we extract the SOI gap Δ_{so}, the TLS dephasing rate γ, as well as the effective spin-photon coupling strength g_{eff} from the dependence of the resonator phase and amplitude on ε. The results are plotted as a function of in-plane angle α in Fig. 3c–e.

Excitingly, we find that, while Δ_{so} and g_{eff} are correlated with each other, they are anticorrelated with γ. In particular, when applying the magnetic field parallel to the NW, a compromise-free sweet spot is found, for which the spin-photon coupling strength g_{eff} is maximal while γ is minimal. To robustly estimate the spin-photon coupling and the dephasing rate at the sweet spot, we average over all extracted values in the interval $\alpha \in [55°, 125°] \cup [235°, 305°]$ and find $\langle g_{eff}\rangle/2\pi = 250 \pm 15(30)$ MHz and $\langle\gamma\rangle/2\pi = 11 \pm 20(400)$ MHz, where the error corresponds to the statistical (systematic) uncertainty. Here, the large systematic uncertainty originates from the uncertainty of the gate lever arms stated in the caption of Table 1.

Theoretical description

In this section, we outline how the effective Hamiltonian yields the dashed white and solid black curves shown in Fig. 3a, c, and d. The consecutive section describes how the decoherence is modeled (black curve in Fig. 3e).

All curves are the result of numerically diagonalizing the Hamiltonian H_5 in Eq. (12) in the Methods that describes the DQD states in proximity to the IDT. Thereby, we take into account an anisotropic g-tensor, identical for both dots, and a spin-orbit vector that is not aligned with the principal axes of the g-tensor. We point out that all curves are obtained from a single set of fit parameter, given in Table 1. The Landé g-factor varies between $g = 10.5$ and $g = 5.25$, depending on the field direction. And, taking into account the distance of the two quantum dots, $d = 330$ nm, the spin-orbit length is found as $l_{so} = 130$ nm. These values are consistent with previous experiments[9,49]. In Methods Section V C, we describe the DQD model in detail and visualize the g-tensor based on the fitted parameters.

After finding the eigenenergies and eigenstates from diagonalizing the Hamiltonian H_5, we focus on the ground state $|0\rangle$ and first excited state $|1\rangle$ with their respective energies E_0 and E_1. These states possess an electric

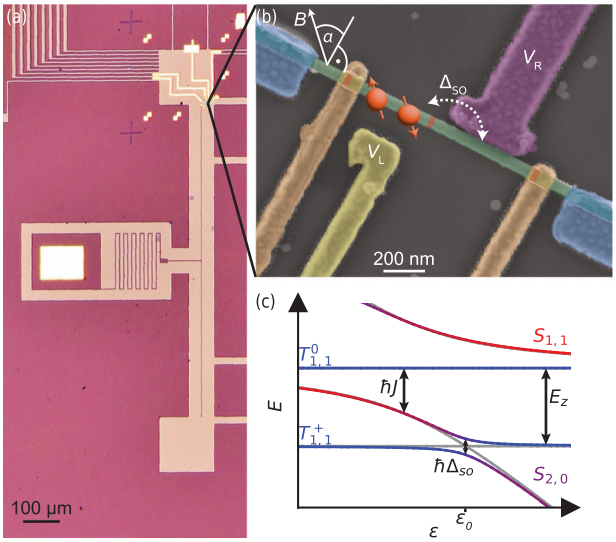

Fig. 1 | Superconducting resonator coupled to singlet-triplet two-level system (TLS) in a crystal-phase nanowire (NW). a Optical microscope image of the device showing a half-wave NbTiN resonator with a characteristic impedance of 2.1 kΩ. In the middle of the center conductor, a dc bias line is connected via a meandered inductor. **b** False-colored scanning electron micrograph of the crystal-phase NW device (image is rotated by − 90° with respect to **a**). The NW is placed at the position indicated in (a), and the purple gate line is galvanically connected to the resonator at its voltage anti-node. Tunnel barriers are highlighted in red. Using the gate voltages V_L and V_R, the device is operated with an even electron filling as depicted schematically. The spin-orbit gap Δ_{SO} corresponds to the indicated spin-rotating tunnel transition, which forms the TLS. The in-plane magnetic field angle α is varied during the experiments using a vector magnet that controls the magnetic field **B**. **c** Level diagram for an even electron occupation as a function of the electrostatic detuning ε in the presence of strong SOI and finite magnetic field exhibiting singlet (S) and triplet (T) states. Subscripts denote the filling of the left and right dots, and the superscript denotes the spin quantum number of the triplet states (see methods). The avoided crossing between the spin-polarized triplet state T^+ and the low-energy singlet state at $\varepsilon = \varepsilon_0$ is detected using the resonator.

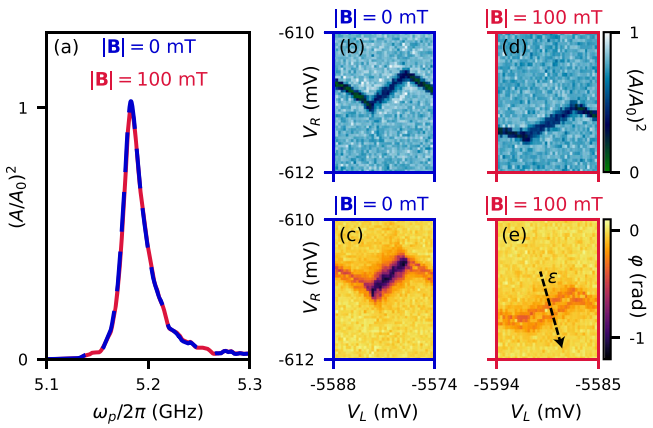

Fig. 2 | Characterization of the hybrid device. a Resonator transmission $(A/A_0)^2$ as function of probe frequency ω_p. Fits to a Lorentzian result in the resonance frequency $\omega_0/2\pi = 5.1854 \pm 0.0002$ GHz, and decay rate $\kappa/2\pi = 21.2 \pm 0.4$ MHz independent of the magnetic-field amplitude |**B**|. The magnetic-field resilience of the resonator enables resonator-based investigation of the double-quantum dot (DQD). **b**–**e** Transmission $(A/A_0)^2$ and phase φ close to resonance frequency as a function of gate voltages V_L and V_R applied to the DQD as illustrated in Fig. 1(b) at zero field and at |**B**| = 100 mT. Position and shape of the observed inter-dot transition signal vary as a function of |**B**| due to an interaction of the resonator with spinful DQD levels. In the remainder of the manuscript, the DQD detuning ε is varied by applying V_L and V_R along the arrow indicated in (e).

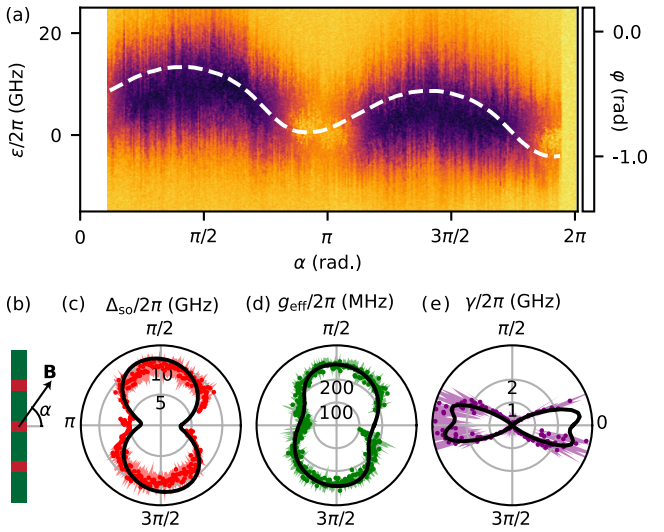

Fig. 3 | Two-level system (TLS) parameters as a function of in-plane field angle at |*B*| = 100 mT. a Phase of the resonator transmission φ as function of electrostatic detuning ε and in-plane magnetic field angle α. The detuning ε, was calculated from the applied voltages, using the gate-to-dot lever arms (see Table 1). The dashed curve corresponds to the position of the inter-dot transition in the theoretical model, $\varepsilon = \varepsilon_0$, to which a linear trend was added accounting for a drift of the gate voltage. **b** Schematic showing the alignment of the magnetic field **B** with respect to the nanowire (NW), where the NW color scheme represents the crystal-phase structure according to Fig. 1b. **c** Spin-orbit gap Δ_{so} as function of α. **d** Coupling strength g_{eff} between the TLS and the resonator as function of α. **e** TLS dephasing rate γ as function of α. When the field is parallel to the NW, $\alpha = \pm\,\pi/2$, a compromise-free sweet spot is found where maximal TLS transition frequency and coupling strength coincide with minimal total dephasing rate. c–e are extracted using input-output theory. The streaks symbolize the uncertainty of the fit. This uncertainty is a consequence of the uncertainty of the gate lever arms, which forms the most significant source of uncertainty in our experiment and is stated in the caption of Table 1. All curves overlaid on the data result from the theoretical model described in the main text, using a single set of fit parameters. During the measurement, a charge relocation occurred at a magnetic-field angle $\alpha \sim 1.9\pi$ resulting in missing data for $\alpha \in [0, 0.1\pi] \cup [0.19\pi, 2\pi)$ in all subfigures.

dipole moment which is sensed by the resonator. Because Eq. (1) is only valid for small SOI, which is not the case for certain field alignments, we more generally determine the detuning ε_0, at which the anti-crossing occurs, by identifying the minimum gap for which

$$\partial_\varepsilon (E_1 - E_0) = 0. \tag{2}$$

The numerical solution for ε_0 is plotted in Fig. 3a on top of the data (white dashed curve). The variations of the detuning ε_0 of the IDT as function of α is caused by the g-tensor anisotropy. According to Eq. (1), this results in a variation of ε_0 at which the Zeeman energy equals the exchange energy. As a consequence, the detuning ε_0 at which the IDT is observed varies with the g-factor, which in turn is given by the field orientation. Then, we numerically calculate the SOI gap

$$\Delta_{so} = E_1(\varepsilon_0) - E_0(\varepsilon_0)\,, \tag{3}$$

plotted as solid black curve in Fig. 3c. The variation of the SOI gap Δ_{so} is a consequence of the magnetic field orientation with respect to the anisotropic g-tensor and the spin-orbit vector. To calculate the vacuum Rabi coupling strength g_{eff}, we assume that the resonator couples to the electric dipole moment of the singlet-triplet TLS via the resonator vacuum fluctuations in the detuning of amplitude $\delta\varepsilon_0$ according to Eq. (11) in the Methods. This

Table 1 | Free parameters

Resonator
Fluctuation amplitude, $\delta\varepsilon_0 = 0.6$
Spin-orbit tensor
Spin-orbit strength, $\Theta_{so} = d/l_{so} = 2.5$
in-plane angle, $\psi = 0.0$ rad
Out-of-plane angle, $\Phi = 2.0$ rad
g-tensor, $\underline{g}$
Maximal g-factor, $g_0 = 10.5$
SOI correction, $\eta = 0.6$
In-plane angle, $\psi_g = 1.3$ rad
Out-of-plane angle, $\Phi_g = 2.0$ rad
Phonons
Phonon-mediated relaxation rate, $\Gamma_{ph}/2\pi = 160$ GHz
Temperature, $T = 100$ mK
Normalized speed of sound,
$c_0 = c/(2\pi r) = (3\ \mathrm{kms}^{-1})/(2\pi \cdot 50\ \mathrm{nm})$
Normalized longitudinal wavefunction extend
$l_0 = l/r = 200\ \mathrm{nm}/50\ \mathrm{nm}$
Normalized distance between wavefunctions
$d_0 = d/r = 300\ \mathrm{nm}/50\ \mathrm{nm}$

Parameters used to fit the data shown in Fig. 3. The tunnel rate $t_c/2\pi = 4.5$ GHz as well as the gate-to-dot lever arms $\alpha_{L2} = 0.014 \pm 0.003$, $\alpha_{L1} = 0.044 \pm 0.008$, $\alpha_{R2} = 0.29 \pm 0.06$ and $\alpha_{R2} = 0.045 \pm 0.014$ were measured independently, where α_{ij} is the dimensionless lever arm between gate i and dot j. The spin-orbit strength Θ_{so} combined with the distance between the dots $d = 300$ nm (center to center) corresponds to a spin-orbit length $l_{so} = d/\Theta_{so} \approx 120$ nm. The last three fit parameters are normalized by the wavefunction radius, $r = 50$ nm.

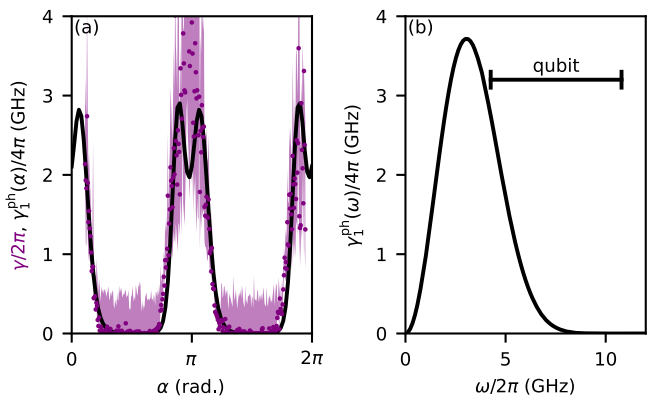

Fig. 4 | Phonons as possible decoherence source. a Measured dephasing rate γ as a function of in-plane angle α (purple). The experimental data is plotted as purple points, and the error bar is given by a purple stripe. The error bars are dominated by the error associated with the gate-lever arm uncertainty. The black curve is the numerically calculated relaxation rate $\gamma_1^{ph}(\alpha)$ originating from deformational phonons (see Section Decoherence). **b** Analytical relaxation rate $\gamma_1^{ph}(\omega)$ as function of phonon frequency ω (see Equation (27) in Supplementary for details). The TLS operates in the frequency range as indicated with a negative slope of $\gamma_1^{ph}(\omega)$. This explains the anti-correlation between the SOI gap Δ_{so} and the dephasing rate γ - a possible reason for the compromise-free sweet spot formation.

gives rise to the dipolar coupling strength as the vacuum Rabi rate

$$g_{\mathrm{eff}} = \delta\varepsilon_0 |\langle 0|h_{\delta\varepsilon}|1\rangle| \tag{4}$$

plotted as solid black curve in Fig. 3d. Here, $h_{\delta\varepsilon}$ is the operator describing small variations of the detuning, given by Eq. (15) in the Methods and evaluated at the center of the IDT, $\varepsilon = \varepsilon_0$.

Decoherence

In the experiment, using input-output theory, we utilize the resonator as a probe to extract the total TLS dephasing rate γ, which is plotted in Fig. 3e, and defined by

$$\gamma = \frac{\gamma_1}{2} + \gamma_\varphi, \tag{5}$$

where γ_1 is the relaxation rate and γ_φ the pure dephasing rate. The primary sources of decoherence in quantum dots are typically hyperfine-interaction induced dephasing from atomic nuclei[50–52], charge noise-induced dephasing[33,34,53,54], or relaxation due to phonons[55–63].

From our experiments, we extract an unexpected anti-correlation between the spin-photon coupling strength g_{eff} and the dephasing rate γ. Using our theoretical description, and Bloch-Redfield theory[56,60,64], we investigate various possible decoherence mechanisms as outlined in the Supplementary Note 2. We find that consideration of magnetic noise stemming from nuclear spins or charge-noise due to phonons leads to the correct trend of γ as a function of the in-plane magnetic-field angle α. However, because we identify dephasing rates comparable to the maximum of $\gamma(\alpha)$ also for a charge qubit at a zero magnetic field, where magnetic noise is irrelevant, we hypothesize that phonons form the dominant noise source in our experiment. Therefore, here, we focus on phonon-mediated decoherence.

Figure 3e and Fig. 4a show the phonon-mediated relaxation $\gamma_1^{ph}(\alpha)$ as a function of the in-plane field angle α overlaid on the measured dephasing rate γ. Considering only the effect of a single gapless, low-energy phonon band gives rise to the analytical functional dependence $\gamma_1^{ph}(\omega)$ as function of phonon frequency, ω. Here, the longitudinal phonon modes couple to the detuning and tunneling through variations in the electrostatic potential due to their deformational interactions. This coupling leads to TLS relaxation (see Supplementary Note 2 for the derivation).

This dependence is plotted in Fig. 4b. These phonons lead to relaxation when their frequency is close to the TLS transition frequency $\omega \approx \Delta_{so}$.

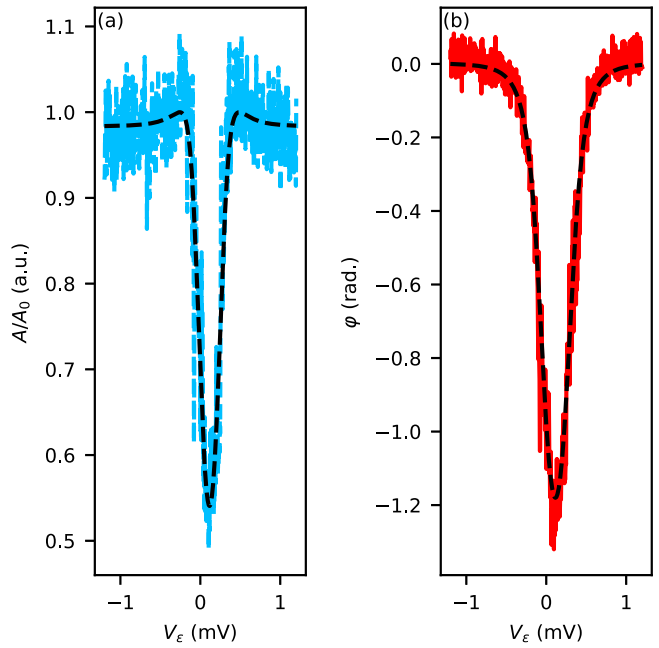

Fig. 5 | Linetrace with input-output theory fit at $\alpha = \pi/2$. a Measured amplitude, A/A_0, as a function of the virtual gate voltage, V_ε which is a linear superposition of the gate voltages V_R and V_L along the detuning direction (arrow in Fig. 2e). Its amplitude is defined such that $|V_\varepsilon| = \sqrt{V_R^2 + V_L^2}$. **b** Measured phase φ as a function of detuning gate voltage V_ε. The data is a linecut of Fig. 3a at $\alpha = \pi/2$. The dashed curves are fits to Eq. (6).

Because the phonon-mediated relaxation is maximal when the phonon wavelength is comparable to the size of the dots at $\omega \approx \omega_c$, an increase in Δ_{so} leads to a decrease in γ_1^{ph}. Therefore, a change in Δ_{so} as function of α results in the observed variations of γ_1^{ph}. In addition, variations of α result in a change of the electron-phonon coupling strength that enhances this effect and is considered in $\gamma_1^{ph}(\alpha)$, plotted as black curve on top of the data in Fig. 4a.

In Supplementary Note 2, we discuss magnetic noise. Additionally, in the Supplementary Note 2, we discuss $1/f$-charge noise, which does not capture the functional dependence of γ as a function of the in-plane magnetic field angle α.

Conclusion

We have investigated a singlet-triplet (S-T$^+$) TLS strongly coupled to a magnetic-field resilient microwave resonator which we use as a sensitive probe. We extract the SOI gap, the vacuum Rabi rate, and the dephasing rate as function of the in-plane magnetic-field orientation. As the central result, we find a compromise-free sweet spot at which the total TLS dephasing rate is minimal while simultaneously its transition frequency and the dipolar coupling to the resonator are maximal. These experimental findings are well described by our theoretical model that shows that at the compromise-free sweet spot, the TLS is resilient against magnetic noise and phonon-mediated noise, with phonons forming the most likely dominant noise source. Fitting the model, we find an anisotropic g-tensor with a maximal g-factor of $g_0 = 10.5$ and a spin-orbit length of $l_{so} = 120$ nm, consistent with literature[9,49]. Our findings demonstrate that, based on the magnetic field as global tuning parameter, optimization of dipole strength and dephasing rate can be not mutually exclusive. Our experimental results and model are very generic and allow for further optimization through synthesis of specifically tailored composite crystals to suppress phonon-induced loss or through a larger resonator frequency. A superconducting resonator combined with input-output theory can be a powerful probe of quantum materials and will enable identifying and optimizing future qubit platforms. Sweet-spot operation might be crucial for large qubit architectures and we anticipate that similar sweet-spots will be identified for qubits in multiple material platforms that rely on large spin-orbit interaction such as hole-spin qubits in Ge[8,26,65–69].

Methods

Device fabrication

The fabrication process commences with the sputter deposition of approximately 10 nm of NbTiN on a pristine Si/SiO_2 wafer[39]. Large structures are patterned utilizing a conventional e-beam protocol and developed at room temperature. Subsequently, the narrow resonator center conductor is patterned in a second e-beam step, followed by development at -20°C[70,71]. Following the dry-etching of the NbTiN film, a NW is deterministically deposited using a micromanipulator. A GaSb-shell that is exclusively present on the zincblende segments of the NW[72,73], allows us to identify the location of the wurtzite tunnel barriers using scanning electron microscopy. After identifying the tunnel barriers, the GaSb shell is removed by wet-etching in MF-319 developer[74]. Consecutively, the contacts and gates are patterned using standard e-beam lithography and thermal evaporation. For the contacts, Ar-milling in the evaporator ensures a good contact, whereas the gates remain isolated by the native oxide on the NW.

Input-output theory

To determine the SOI gap Δ_{so}, the effective spin-photon coupling strength g_{eff}, and the TLS dephasing rate γ, we make use of input-output theory that describes the interaction between photons in a resonator and a multi-level system[48,75]. Input-output theory allows us to infer the transition frequency, vacuum Rabi rate and dephasing rate of two-level systems formed in a DQD[21,22,76–81]. For the singlet-triplet (S-T+) TLS coupled to a resonator, which is probed in transmission at low power, the linear response of the measured scattering parameter is derived as[22,82]

$$S_{21}(\omega) = \frac{-i\kappa}{\omega - \omega_0 + i\frac{\kappa}{2} - g^2\left(\frac{1}{\omega-\omega_q+i\gamma} - \frac{1}{\omega+\omega_q+i\gamma}\right)}, \tag{6}$$

where $\omega_q = \sqrt{\Delta_{so}^2 + \varepsilon'^2}$, with $\varepsilon' = \varepsilon - \varepsilon_0$ the relative electrostatic DQD detuning from the center of the IDT and $g = g_{eff}\Delta_{so}/\omega_q$. ω_0 and κ denote the bare resonator frequency and resonator decay rate and γ is the TLS dephasing. Here we do not apply the usual rotating-wave approximation, preserving the counter-rotating terms, that are relevant for large frequency detuning $|\omega_q - \omega_0| \ll |\omega_q + \omega_0|$. To obtain the fit parameters plotted in Fig. 3c–e for every value of field angle α, we fit amplitude and phase of Eq. (6) simultaneously to the measured amplitude and phase as a function of detuning ε. Figure 5 shows amplitude and phase at $\alpha = \pi/2$ of the measurement shown in Fig. 3 with the overlaid fit. From this fit, we extract the SOI gap Δ_{so}, the coupling strength g_{eff}, and the dephasing rate γ. Repeating a similar procedure for various values of α results in the plots in Fig. 3c–e. The frequency of the resonator ω_0 and the decay rate of the resonator κ as well as the lever arm, which transforms the applied gate voltages into detuning, are determined independently and kept fixed for the fit. When extracting three fit parameters simultaneously, it is crucial to avoid overfitting. In this study, we address the risk of overfitting by fitting both amplitude and phase using a single set of fit parameters. This method results in small point-to-point fluctuations and very small error bars on the extracted parameters, giving us certainty that the fit is accurate. However, these error bars do not fully represent the physical uncertainty of the measurements. The primary source of uncertainty in our experiments arises from the error associated with the gate-lever arm. To determine the error bars shown in Figs. 3 and 4, we propagate the uncertainty of the gate-lever arm through the fitting process and then calculate the two-point systematics.

Model of the double quantum dot

The curves plotted in Figs. 3 and 4 of the main text are the result of numerical diagonalization of the effective Hamiltonian of a double quantum dot (DQD) with even occupation close to the avoided crossing between $|T_{1,1}^+\rangle$ and $|S_{2,0}\rangle$. Here, for a symbol $A_{l,r}^i$, $A = S$ denotes the anti-symmetric spin

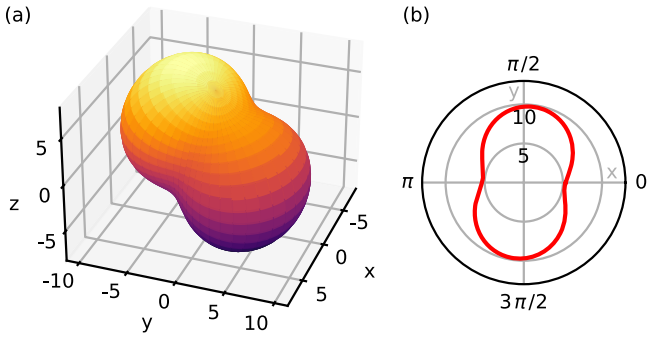

Fig. 6 | Visualization of the anisotropic g-tensor. a Normalized Zeeman field strength $|\mathbf{B}\underline{g}|/|\mathbf{B}|$, where the g-tensor $\underline{g}$ is defined according to Eq. (10). A characteristic peanut shape is exhibited. **b** Cross-section of a in the *x*-*y* plane at $z = 0$ as a function of the in-plane angle α. The nanowire is aligned parallel to the *y* axis.

singlet state $|S\rangle = (|\uparrow\downarrow\rangle - |\downarrow\uparrow\rangle)/\sqrt{2}$. $A = T$ denotes the symmetric triplet states, where $|T^+\rangle = |\uparrow\uparrow\rangle$, and $|T^-\rangle = |\downarrow\downarrow\rangle$ are spin-polarized and $|T^0\rangle = (|\uparrow\downarrow\rangle + |\downarrow\uparrow\rangle)/\sqrt{2}$ is unpolarized. In our notation, the Zeeman field points in the $-z$ direction. The subscripts l, r denote the charge occupation of the left and right dot. The $(1,1) \to (0,2)$ anticrossing is driven by changing the detuning ε between the two dots. For the usual negative exchange splitting between the S and T states, the (1,1) state is preferred at $\varepsilon < 0$ and the state (2,0) is preferred at $\varepsilon > 0$.

The singlet and triplet states in the DQD are $(|S_{0,2}\rangle, |S_{2,0}\rangle, |S_{1,1}\rangle, |T^-_{1,1}\rangle, |T^+_{1,1}\rangle, |T^0_{1,1}\rangle)$ and form our basis set. The Hamiltonian including SOI then reads[24,32,83]

$$H_{\mathrm{DQD}} = \begin{pmatrix} U_L + U_R + \varepsilon & U_{LR} & -t_c & 0 & 0 & 0 \\ U_{LR} & -\varepsilon & -t_c & 0 & 0 & 0 \\ -t_c & -t_c & -J_0 & -\frac{\delta b_x + i\delta b_y}{\sqrt{2}} & \frac{\delta b_x - i\delta b_y}{\sqrt{2}} & \delta b_z \\ 0 & 0 & -\frac{\delta b_x - i\delta b_y}{\sqrt{2}} & \bar{b}_z & 0 & \frac{\bar{b}_x - i\bar{b}_y}{\sqrt{2}} \\ 0 & 0 & \frac{\delta b_x + i\delta b_y}{\sqrt{2}} & 0 & -\bar{b}_z & \frac{\bar{b}_x + i\bar{b}_y}{\sqrt{2}} \\ 0 & 0 & \delta b_z & \frac{\bar{b}_x + i\bar{b}_y}{\sqrt{2}} & \frac{\bar{b}_x - i\bar{b}_y}{\sqrt{2}} & 0 \end{pmatrix}. \tag{7}$$

Here, $U_{L/R}$ is the on-site Coulomb energy of the left (L) and right (R) dot, U_{LR} is the cross-exchange contribution, and J_0 is the Coulomb exchange. And we define the difference and total Zeeman field vectors produced by a magnetic field $\mathbf{B}$ as

$$\delta\mathbf{b} = \mu_B \mathbf{B} \delta g = \frac{\mu_B}{2} \mathbf{B} \left[\underline{g}_L \underline{R}(-\theta_{so}/2) - \underline{g}_R \underline{R}(\theta_{so}/2) \right], \tag{8}$$

$$\bar{\mathbf{b}} = \mu_B \mathbf{B} \bar{g} = \frac{\mu_B}{2} \mathbf{B} \left[\underline{g}_L \underline{R}(-\theta_{so}/2) + \underline{g}_R \underline{R}(\theta_{so}/2) \right], \tag{9}$$

where $\underline{R}$ is a rotation matrix around the SOI axis by the spin-flip angle $\theta_{so} = d/l_{so}$, with d the distance between the dots and l_{so} the SOI length. For simplicity, we set $U_{LR} = J_0 = 0$. Following Ref. 32, we have gauged the spin-flip tunneling contribution into a local redefinition of the Zeeman energy and thus the tunneling amplitude t_c comprises both spin-conserving and spin-flip components. $\underline{g}_{L/R}$ are the g-tensors of the left and right dots, parameterized by the unit vector $\mathbf{n}$ and the SOI correction factor $\eta \leq 1$,

$$\mathbf{B}\underline{g} = g_0 \left[(\mathbf{n}(\mathbf{n} \cdot \mathbf{B})) + \eta (\mathbf{n} \times \mathbf{B}) \times \mathbf{n} \right]. \tag{10}$$

For describing the experimental results and to limit the number of free parameters, we use identical g-tensors for the left and right dot, $\underline{g} = \underline{g}_L = \underline{g}_R$. A visualization of these g-tensors, based on the Equation (10) and the fit parameters, is shown in Fig. 6.

The DQD is coupled to a resonator of frequency ω_0 and bosonic annihilation and creation operators a and $a^\dagger$, with the effective Hamiltonian $H_R = \hbar\omega_0 a^\dagger a$. The coupling is mediated by the resonator-induced change in detuning of the DQD and thus reads

$$H_I = \delta\varepsilon(|S_{20}\rangle\langle S_{20}| - |S_{02}\rangle\langle S_{02}|)(a^\dagger + a), \tag{11}$$

where $\delta\varepsilon = V_R \partial_V \varepsilon$ depends on the susceptibility of the detuning to the potential applied to the gate and on the zero-point-fluctuations V_R of the potential of the resonator.

Focusing on the $(1,1) \to (0,2)$ anticrossing at $\varepsilon \sim \varepsilon_0$, we neglect the contribution of the singlet $|S_{20}\rangle$ which lies at high energy $U_R + U_L$. We can then easily diagonalize the singlet subsector by accounting for the tunneling between S_{11} and S_{20}, and we focus on the 5 lowest energy states of the system, comprising the resulting singlets and the three triplets. The effective Hamiltonian reads

$$H_5 = \begin{pmatrix} J - \varepsilon & 0 & -\frac{(\delta b'_x + i\delta b'_y)\cos(\theta)}{\sqrt{2}} & \frac{(\delta b'_x - i\delta b'_y)\cos(\theta)}{\sqrt{2}} & \delta b'_z \cos(\theta) \\ 0 & -J & -\frac{(\delta b'_x + i\delta b'_y)\sin(\theta)}{\sqrt{2}} & \frac{(\delta b'_x - i\delta b'_y)\sin(\theta)}{\sqrt{2}} & \delta b'_z \sin(\theta) \\ -\frac{(\delta b'_x - i\delta b'_y)\cos(\theta)}{\sqrt{2}} & -\frac{(\delta b'_x - i\delta b'_y)\sin(\theta)}{\sqrt{2}} & E_z & 0 & 0 \\ \frac{(\delta b'_x + i\delta b'_y)\cos(\theta)}{\sqrt{2}} & \frac{(\delta b'_x + i\delta b'_y)\sin(\theta)}{\sqrt{2}} & 0 & -E_z & 0 \\ \delta b'_z \cos(\theta) & \delta b'_z \sin(\theta) & 0 & 0 & 0 \end{pmatrix}, \tag{12}$$

where $J \approx (\varepsilon + \sqrt{\varepsilon^2 + 4t_c^2})/2$ according to Eq. (1) and $\theta = \arctan(2t_c/\varepsilon)/2$, where the arctan function is defined, such that $\theta = \pi/4$ at $\varepsilon = 0$. We also fixed the direction of the spin quantization axis such that the triplet subsector is diagonal. This is done by defining the global rotation matrix $\underline{R}_B$ that maps $\bar{\mathbf{b}}$ to the *z*-direction and rotating the $\delta\mathbf{b}$ accordingly, i.e.,

$$\bar{\mathbf{b}} = E_z \underline{R}_B \mathbf{n}_z \;\to\; \delta\mathbf{b}' = \delta\mathbf{b}\underline{R}_B. \tag{13}$$

Here, $\underline{R}_B$ depends on the direction of the applied $\mathbf{B}$ field and on the combined g-tensor of the dots. The prime in $\delta\mathbf{b}$ indicates this choice of reference frame for the spin quantization axis.

The resonator-DQD coupling Hamiltonian H_I in Eq. (11) is related to variations in the detuning $\delta\epsilon$ by

$$H_I = \delta\varepsilon_0 h_\varepsilon (a^\dagger + a), \tag{14}$$

with

$$h_\varepsilon = \begin{pmatrix} -\sin^2(\theta) & \sin(2\theta)/2 & 0 & 0 & 0 \\ \sin(2\theta)/2 & -\cos^2(\theta) & 0 & 0 & 0 \\ 0 & 0 & 0 & 0 & 0 \\ 0 & 0 & 0 & 0 & 0 \\ 0 & 0 & 0 & 0 & 0 \end{pmatrix} \tag{15}$$

describing small variations of the detuning ε. This leads to the definition of the dipolar coupling strength according to Eq. (4).

Data availability

The numerical data used in this study are available in the zenodo database https://doi.org/10.5281/zenodo.11205195.

Received: 14 May 2025; Accepted: 3 July 2025;
Published online: 23 July 2025

References

1. Hanson, R., Kouwenhoven, L. P., Petta, J. R., Tarucha, S. & Vandersypen, L. M. K. Spins in few-electron quantum dots. *Rev. Mod. Phys.* **79**, 1217–1265 (2007).

2. Veldhorst, M. et al. An addressable quantum dot qubit with fault-tolerant control-fidelity. *Nat. Nanotechnol.* **9**, 981–985 (2014).
3. Yoneda, J. et al. Robust micromagnet design for fast electrical manipulations of single spins in quantum dots. *Appl. Phys. Express* **8**, 084401 (2015).
4. Bulaev, D. V. & Loss, D. Spin relaxation and decoherence of holes in quantum dots. *Phys. Rev. Lett.* **95**, 076805 (2005).
5. Bulaev, D. V. & Loss, D. Electric dipole spin resonance for heavy holes in quantum dots. *Phys. Rev. Lett.* **98**, 097202 (2007).
6. Maurand, R. et al. A CMOS silicon spin qubit. *Nat. Commun.* **7**, 13575 (2016).
7. Watzinger, H. et al. A germanium hole spin qubit. *Nat. Commun.* **9**, 3902 (2018).
8. Froning, F. N. et al. Ultrafast hole spin qubit with gate-tunable spin–orbit switch functionality. *Nat. Nanotechnol.* **16**, 308–312 (2021).
9. Nadj-Perge, S., Frolov, S. M., Bakkers, E. Pa. M. & Kouwenhoven, L. P. Spin-orbit qubit in a semiconductor nanowire. *Nature* **468**, 1084–1087 (2010).
10. Schroer, M. D., Petersson, K. D., Jung, M. & Petta, J. R. Field tuning the *g* factor in inas nanowire double quantum dots. *Phys. Rev. Lett.* **107**, 176811 (2011).
11. Petersson, K. D. et al. Circuit quantum electrodynamics with a spin qubit. *Nature* **490**, 380–383 (2012).
12. van Weperen, I. et al. Spin-orbit interaction in InSb nanowires. *Phys. Rev. B* **91**, 201413 (2015).
13. Han, L. et al. Variable and orbital-dependent spin-orbit field orientations in an insb double quantum dot characterized via dispersive gate sensing. *Phys. Rev. Appl.* **19**, 014063 (2023).
14. Rashba, E. & Efros, A. L. Orbital mechanisms of electron-spin manipulation by an electric field. *Phys. Rev. Lett.* **91**, 126405 (2003).
15. Golovach, V. N., Borhani, M. & Loss, D. Electric-dipole-induced spin resonance in quantum dots. *Phys. Rev. B* **74**, 165319 (2006).
16. Nowack, K. C., Koppens, F., Nazarov, Y. V. & Vandersypen, L. Coherent control of a single electron spin with electric fields. *Science* **318**, 1430–1433 (2007).
17. Van den Berg, J. et al. Fast spin-orbit qubit in an indium antimonide nanowire. *Phys. Rev. Lett.* **110**, 066806 (2013).
18. Kloeffel, C., Trif, M., Stano, P. & Loss, D. Circuit qed with hole-spin qubits in ge/si nanowire quantum dots. *Phys. Rev. B* **88**, 241405 (2013).
19. Crippa, A. et al. Gate-reflectometry dispersive readout and coherent control of a spin qubit in silicon. *Nat. Commun.* **10**, 2776 (2019).
20. Bosco, S., Scarlino, P., Klinovaja, J. & Loss, D. Fully tunable longitudinal spin-photon interactions in si and ge quantum dots. *Phys. Rev. Lett.* **129**, 066801 (2022).
21. Yu, C. X. et al. Strong coupling between a photon and a hole spin in silicon. *Nat. Nanotechnol.* **18**, 741–746 (2023).
22. Ungerer, J. H. et al. Strong coupling between a microwave photon and a singlet-triplet qubit. *Nat. Commun.* **15**, 1068 (2024).
23. De Palma, F. *et al*. Strong hole-photon coupling in planar ge: probing the charge degree and wigner molecule states. *arXiv:2310.20661* https://arxiv.org/abs/2310.20661 (2023).
24. Stepanenko, D., Rudner, M., Halperin, B. I. & Loss, D. Singlet-triplet splitting in double quantum dots due to spin-orbit and hyperfine interactions. *Phys. Rev. B* **85**, 075416 (2012).
25. Nichol, J. M. et al. Quenching of dynamic nuclear polarization by spin-orbit coupling in GaAs quantum dots. *Nat. Commun.* **6**, 7682 (2015).
26. Jirovec, D. et al. A singlet-triplet hole spin qubit in planar ge. *Nat. Mater.* **20**, 1106–1112 (2021).
27. Samkharadze, N. et al. Strong spin-photon coupling in silicon. *Science* **359**, 1123–1127 (2018).
28. Mi, X. et al. A coherent spin-photon interface in silicon. *Nature* **555**, 599–603 (2018).
29. Landig, A. J. et al. Coherent spin-photon coupling using a resonant exchange qubit. *Nature* **560**, 179–184 (2018).
30. Piot, N. et al. A single hole spin with enhanced coherence in natural silicon. *Nat. Nanotechnol.* **17**, 1072–1077 (2022).
31. d'Hollosy, S., Fábián, G., Baumgartner, A., Nygård, J. & Schönenberger, C. g-factor anisotropy in nanowire-based inas quantum dots. In *AIP Conference Proceedings*, vol. 1566, 359–360 (American Institute of Physics, 2013). https://pubs.aip.org/aip/acp/article-abstract/1566/1/359/880995/g-factor-anisotropy-in-nanowire-based-InAs-quantum.
32. Geyer, S. et al. Anisotropic exchange interaction of two hole-spin qubits. *Nat. Phys.* **20**, 1152–1157 (2024).
33. Petersson, K., Petta, J., Lu, H. & Gossard, A. Quantum coherence in a one-electron semiconductor charge qubit. *Phys. Rev. Lett.* **105**, 246804 (2010).
34. Scarlino, P. et al. In situ tuning of the electric-dipole strength of a double-dot charge qubit: charge-noise protection and ultrastrong coupling. *Phys. Rev. X* **12**, 031004 (2022).
35. Carballido, M. J. et al. A qubit with simultaneously maximized speed and coherence. *arXiv:2402.07313* https://arxiv.org/abs/2402.07313 (2024).
36. Lehmann, S., Wallentin, J., Jacobsson, D., Deppert, K. & Dick, K. A. A general approach for sharp crystal phase switching in InAs, GaAs, InP, and GaP nanowires using only Group V Flow. *Nano Lett.* **13**, 4099–4105 (2013).
37. Nilsson, M. et al. Single-electron transport in InAs nanowire quantum dots formed by crystal phase engineering. *Phys. Rev. B* **93**, 195422 (2016).
38. Samkharadze, N. et al. High-kinetic-inductance superconducting nanowire resonators for circuit QED in a magnetic field. *Phys. Rev. Appl.* **5**, 044004 (2016).
39. Ungerer, J. H. et al. Performance of high impedance resonators in dirty dielectric environments. *EPJ Quantum Technol.* **10**, 1–13 (2023).
40. Tanttu, T. et al. Controlling spin-orbit interactions in silicon quantum dots using magnetic field direction. *Phys. Rev. X* **9**, 021028 (2019).
41. Jünger, C. et al. Magnetic-field-independent subgap states in hybrid rashba nanowires. *Phys. Rev. Lett.* **125**, 017701 (2020).
42. Stockklauser, A. et al. Strong coupling cavity qed with gate-defined double quantum dots enabled by a high impedance resonator. *Phys. Rev. X* **7**, 011030 (2017).
43. Schroer, M., Jung, M., Petersson, K. & Petta, J. R. Radio frequency charge parity meter. *Phys. Rev. Lett.* **109**, 166804 (2012).
44. Malinowski, F. K. et al. Spin of a multielectron quantum dot and its interaction with a neighboring electron. *Phys. Rev. X* **8**, 011045 (2018).
45. Ezzouch, R. et al. Dispersively probed microwave spectroscopy of a silicon hole double quantum dot. *Phys. Rev. Appl.* **16**, 034031 (2021).
46. Frey, T. et al. Dipole coupling of a double quantum dot to a microwave resonator. *Phys. Rev. Lett.* **108**, 046807 (2012).
47. Hendrickx, N. et al. Sweet-spot operation of a germanium hole spin qubit with highly anisotropic noise sensitivity. *arXiv:2305.13150* https://arxiv.org/abs/2305.13150 (2023).
48. Gardiner, C. W. & Collett, M. J. Input and output in damped quantum systems: Quantum stochastic differential equations and the master equation. *Phys. Rev. A* **31**, 3761 (1985).
49. Fasth, C., Fuhrer, A., Samuelson, L., Golovach, V. N. & Loss, D. Direct measurement of the spin-orbit interaction in a two-electron inas nanowire quantum dot. *Phys. Rev. Lett.* **98**, 266801 (2007).
50. Assali, L. V. et al. Hyperfine interactions in silicon quantum dots. *Phys. Rev. B* **83**, 165301 (2011).
51. Schliemann, J., Khaetskii, A. & Loss, D. Electron spin dynamics in quantum dots and related nanostructures due to hyperfine interaction with nuclei. *J. Phys.: Condens. Matter* **15**, R1809 (2003).
52. Testelin, C., Bernardot, F., Eble, B. & Chamarro, M. Hole–spin dephasing time associated with hyperfine interaction in quantum dots. *Phys. Rev. B* **79**, 195440 (2009).

53. Holman, N. et al. 3d integration and measurement of a semiconductor double quantum dot with a high-impedance tin resonator. *npj Quantum Inf.* **7**, 137 (2021).
54. Paladino, E., Galperin, Y., Falci, G. & Altshuler, B. 1/f noise: Implications for solid-state quantum information. *Rev. Mod. Phys.* **86**, 361 (2014).
55. Fujisawa, T. et al. Spontaneous emission spectrum in double quantum dot devices. *Science* **282**, 932–935 (1998).
56. Golovach, V. N., Khaetskii, A. & Loss, D. Phonon-induced decay of the electron spin in quantum dots. *Phys. Rev. Lett.* **93**, 016601 (2004).
57. Trif, M., Golovach, V. N. & Loss, D. Spin dynamics in inas nanowire quantum dots coupled to a transmission line. *Phys. Rev. B* **77**, 045434 (2008).
58. Kornich, V., Kloeffel, C. & Loss, D. Phonon-mediated decay of singlet-triplet qubits in double quantum dots. *Phys. Rev. B* **89**, 085410 (2014).
59. Kloeffel, C., Trif, M. & Loss, D. Acoustic phonons and strain in core/shell nanowires. *Phys. Rev. B* **90**, 115419 (2014).
60. Kornich, V., Kloeffel, C. & Loss, D. Phonon-assisted relaxation and decoherence of singlet-triplet qubits in si/sige quantum dots. *Quantum* **2**, 70 (2018).
61. Hartke, T., Liu, Y.-Y., Gullans, M. & Petta, J. Microwave detection of electron-phonon interactions in a cavity-coupled double quantum dot. *Phys. Rev. Lett.* **120**, 097701 (2018).
62. Hofmann, A. et al. Phonon spectral density in a gaas/algaas double quantum dot. *Phys. Rev. Res.* **2**, 033230 (2020).
63. Zou, J., Bosco, S. & Loss, D. Spatially correlated classical and quantum noise in driven qubits. *npj Quantum Inf.* **10**, 46 (2024).
64. Cywiński, Ł., Lutchyn, R. M., Nave, C. P. & Sarma, S. D. How to enhance dephasing time in superconducting qubits. *Phys. Rev. B* **77**, 174509 (2008).
65. Hendrickx, N. et al. A single-hole spin qubit. *Nat. Commun.* **11**, 3478 (2020).
66. Zhang, X. et al. Universal control of four singlet-triplet qubits. *arXiv:2312.16101* https://arxiv.org/abs/2312.16101 (2023).
67. Wang, C.-A. et al. Operating semiconductor quantum processors with hopping spins. *Science* **385**, 447–452 (2024).
68. Zhang, X. et al. Universal control of four singlet–triplet qubits. *Nat. Nanotechnol.* **20**, 209–215 (2025).
69. Saez-Mollejo, J. et al. Microwave driven singlet-triplet qubits enabled by site-dependent g-tensors. *arXiv preprint arXiv:2408.03224* (2024).
70. Ridderbos, J.*Quantum dots and superconductivity in Ge-Si nanowires*. Ph.D. thesis, University of Twente https://ris.utwente.nl/ws/portalfiles/portal/24823430/ (2018).
71. Ungerer, J. H.*High-impedance circuit quantum electrodynamics with semiconductor quantum dots*. Ph.D. thesis, University of Basel https://edoc.unibas.ch/95248/ (2023).
72. Gatzke, C., Webb, S., Fobelets, K. & Stradling, R. In situ raman spectroscopy of the selective etching of antimonides in gasb/alsb/inas heterostructures. *Semicond. Sci. Technol.* **13**, 399 (1998).
73. Barker, D. et al. Individually addressable double quantum dots formed with nanowire polytypes and identified by epitaxial markers. *Appl. Phys. Lett.***114** https://pubs.aip.org/aip/apl/article-abstract/114/18/183502/36814/Individually-addressable-double-quantum-dots (2019).
74. Pally, A. P. *Crystal-phase defined nanowire quantum dots as a platform for qubits*. Ph.D. thesis, University of Basel https://edoc.unibas.ch/96320/ (2024).
75. Benito, M., Mi, X., Taylor, J. M., Petta, J. R. & Burkard, G. Input-output theory for spin-photon coupling in Si double quantum dots. *Phys. Rev. B* **96**, 235434 (2017).
76. Burkard, G. & Petta, J. R. Dispersive readout of valley splittings in cavity-coupled silicon quantum dots. *Phys. Rev. B* **94**, 195305 (2016).
77. Mi, X., Péterfalvi, C. G., Burkard, G. & Petta, J. R. High-resolution valley spectroscopy of si quantum dots. *Phys. Rev. Lett.* **119**, 176803 (2017).
78. Borjans, F. et al. Probing the variation of the intervalley tunnel coupling in a silicon triple quantum dot. *PRX Quantum* **2**, 020309 (2021).
79. Ibberson, D. J. et al. Large dispersive interaction between a cmos double quantum dot and microwave photons. *PRX Quantum* **2**, 020315 (2021).
80. Ruckriegel, M. J. et al. Dipole coupling of a bilayer graphene quantum dot to a high-impedance microwave resonator. *arXiv:2312.14629* https://arxiv.org/abs/2312.14629 (2023).
81. Ranni, A. et al. Dephasing in a crystal-phase defined double quantum dot charge qubit strongly coupled to a high-impedance resonator. *arXiv:2308.14887* https://arxiv.org/abs/2308.14887 (2023).
82. Kohler, S. Dispersive readout: Universal theory beyond the rotating-wave approximation. *Phys. Rev. A* **98**, 023849 (2018).
83. Spethmann, M., Bosco, S., Hofmann, A., Klinovaja, J. & Loss, D. High-fidelity two-qubit gates of hybrid superconducting-semiconducting singlet-triplet qubits. *Phys. Rev. B* **109**, 085303 (2024).

Acknowledgements

We are grateful for fruitful discussions with J. Danon, A. Ranni, C. Reissel and C. Ventura Meinersen. The research was supported by the Swiss Nanoscience Institute (SNI), and the Swiss National Science Foundation through grant 192027. This work was supported by the Swiss National Science Foundation, NCCR SPIN (Grant number 51NF40-180604). We further acknowledge funding from the European Union's Horizon 2020 research and innovation program, specifically the FET-open project AndQC, agreement No 828948 and the FET-open project TOPSQUAD, agreement No 847471. We also acknowledge support through the Marie Skłodowska -Curie COFUND grant QUSTEC, grant agreement N° 847471 and the Basel Quantum Center through a Georg H. Endress fellowship. We furthermore acknowledge support from NanoLund. P.S. acknowledges support from the Swiss National Science Foundation through Projects No. 200021_200418, and from the Swiss State Secretariat for Education, Research and Innovation (SERI) under contract number MB22.00081.

Author contributions

S.L. grew the nanowire with contributions from C.T. J.H.U. and A.P. fabricated the device with support from D.S. and A.K. J.H.U., A.P., and A.K. performed the measurements. S.B. formulated the theoretical model with contributions from D.L. J.H.U., A.P., and S.B. analyzed the data with input from V.F.M., A.B., P.S., and C.S. J.H.U. wrote the manuscript with contributions from all authors. C.S. supervised the project.

Competing interests

All authors declare no competing interests.

Additional information

Supplementary information The online version contains supplementary material available at https://doi.org/10.1038/s42005-025-02216-9.

Correspondence and requests for materials should be addressed to Jann H. Ungerer.

Peer review information This manuscript has been previously reviewed at another journal that is not operating a transparent peer review scheme. The manuscript was considered suitable for publication without further review at *Communications Physics*.

Reprints and permissions information is available at http://www.nature.com/reprints

Publisher's note Springer Nature remains neutral with regard to jurisdictional claims in published maps and institutional affiliations.

Open Access This article is licensed under a Creative Commons Attribution-NonCommercial-NoDerivatives 4.0 International License, which permits any non-commercial use, sharing, distribution and reproduction in any medium or format, as long as you give appropriate credit to the original author(s) and the source, provide a link to the Creative Commons licence, and indicate if you modified the licensed material. You do not have permission under this licence to share adapted material derived from this article or parts of it. The images or other third party material in this article are included in the article's Creative Commons licence, unless indicated otherwise in a credit line to the material. If material is not included in the article's Creative Commons licence and your intended use is not permitted by statutory regulation or exceeds the permitted use, you will need to obtain permission directly from the copyright holder. To view a copy of this licence, visit http://creativecommons.org/licenses/by-nc-nd/4.0/.

© The Author(s) 2025